agriculture

*Article*

# Effect of Preparation Process on the Physicochemical Properties of Activated Carbon Prepared from Corn Stalks

**Beibei Xu [1], Min Chang [1], Chengguo Fu [1], Jiale Han [1], Yahui Wang [1], Yipeng Feng [1,2,*] and Zhiping Zhang [2]**

[1] School of Mechanical and Electrical Engineering, Henan Institute of Science and Technology, Xinxiang 453003, China; 15729233575@163.com (B.X.); 13569853703@163.com (M.C.); scu_fcg@163.com (C.F.); hanjiale407@163.com (J.H.); yhwang1986@foxmail.com (Y.W.)

[2] Key Laboratory of New Materials and Facilities for Rural Renewable Energy of China's Ministry of Agriculture and Rural Affairs, Henan Agricultural University, Zhengzhou 450002, China; zhangzhiping715@163.com

* Correspondence: fengyipeng0001@126.com

**Abstract:** The preparation of activated carbon (AC) from agricultural and forestry wastes is one of the effective methods for resource utilization. In this study, AC was prepared from corn stalk (CS) by pyrolysis, one-step activation, and two-step activation to determine the optimum preparation method. Based on this, a single-factor design was used to investigate the influence of activating agents (KOH, NaOH, KOH/NaOH), activation temperatures (600, 700, 800 °C), and activation times (60, 90, 120 min) on the physicochemical properties of AC. The physicochemical properties of AC were characterized by Thermal gravimetric analysis (TGA), Fourier-transform infrared spectroscopy (FTIR), X-ray diffraction (XRD), Scanning electron microscopy (SEM), and Cyclic voltammetry (CV). The results showed that the AC obtained by the one-step activation method (KOH, 800 °C, 120 min) exhibited a rich pore structure and excellent electrochemical properties ($I_{pa}$ = 159.8 μA, $I_{pc}$ = −169.5 μA). However, for the two-step activation method, the AC exhibited a poor pore structure and electrochemical properties ($I_{pa}$ = 130.8 μA, $I_{pc}$ = −129.9 μA). In addition, one-step activation provides high-quality AC in a shorter activation time than two-step activation.

**Keywords:** corn stalk; activated carbon; preparation method; activation temperature; activating agent; activation time

**Citation:** Xu, B.; Chang, M.; Fu, C.; Han, J.; Wang, Y.; Feng, Y.; Zhang, Z. Effect of Preparation Process on the Physicochemical Properties of Activated Carbon Prepared from Corn Stalks. *Agriculture* **2024**, *14*, 392. https://doi.org/10.3390/agriculture14030392

Academic Editors: Zhongqi Cheng and Vincenzo Alfano

Received: 19 December 2023
Revised: 17 February 2024
Accepted: 28 February 2024
Published: 29 February 2024



## 1. Introduction

Biomass is primarily composed of cellulose, hemicellulose, and lignin, with carbon (C), hydrogen (H), and oxygen (O) comprising for 70% to 90% of its elemental composition [1–3]. After pyrolysis and carbonization, biomass produces flakes of carbon and coke leach, while releasing $H_2O$, CO, $CH_4$, and other volatile chemicals [4]. Activated carbon materials are favored for their excellent adsorption capacity, superior chemical stability and electrochemical properties [5,6]. Nowadays, it is widely used in heavy metal adsorption, wastewater treatment, supercapacitors [7–10]. Various biomass wastes can be used to prepare activated carbon (AC), such as peanut shells [11], oil palm kernel shells [12], rice husks [13] and orange peels [14]. The preparation of activated carbon from biomass waste not only solves the problem of waste treatment, but also realizes the recycling of resources and environmental protection. Due to the wide range of applications of activated carbon in various fields, its preparation process has become one of the hot topics of research.

Although the traditional pyrolysis method is operationally simple, there are limitations in the properties of the pyrolyzed carbon obtained. To overcome these shortcomings, new methods such as hydrothermal carbonization [15], microwave heating [16], template method [17], and chemical activation method [18] have been rapidly developed in recent

years. It is worth noting that chemical activation method has the advantages such as low heating temperature, a short processing time, and high carbon production rate, which are significantly prominent in enhancing the performance of activated carbon. Chemical activation can be categorized into one-step activation and two-step activation, providing more flexible options for activated carbon preparation [19]. One-step activation is the simultaneous carbonization and activation of biomass in a single reaction process [20]. Yin et al. [21] used the one-step activation of rice straw to obtain activated carbon with a larger surface area and abundant functional groups. Lin et al. [22] also used one-step activation to obtain activated carbon with excellent specific capacitance from hemicellulose. In contrast, the two-step activation first carbonizes the precursor and then thoroughly mixes the carbon the activating agent for activation [23]. Jiang et al. [24] used chestnut shell waste to obtain activated carbon with superior capacitance properties through two-step activation. Mistar et al. [25] utilized bambusa vulgaris striata as the precursor and successfully produced AC with excellent porosity through a two-step activation process using KOH. Although researchers have utilized both one-step and two-step activation methods for the preparation of AC, there has been a lack of comprehensive and detailed comparative studies between these two approaches.

Hence, in this study, corn stalks were used as raw materials to prepare AC through pyrolysis, one-step activation, and two-step activation. The influence of activation temperature, activating agent, and activation time on the physicochemical properties of AC were investigated by a single-factor design. In this study, the physical and chemical properties of AC were comprehensively characterized, including thermal decomposition behavior, microstructure, crystal structure and electrochemical properties. These characterizations help determine the optimal conditions for the preparation of activated carbon. By analyzing the properties of activated carbon, some experience and knowledge were obtained, which provided practical suggestions for the efficient preparation of high-quality activated carbon from biomass waste.

## 2. Material and Methods

### *2.1. Materials*

In this study, corn stalks (CSs) were harvested from the region of Henan Province, China. The CSs were rinsed with deionized water to remove dust and impurities from CS before use (no variation in chemical composition after rinsing). Subsequently, the CSs were placed in an 80 °C oven and dried for a duration of 12 h. CSs were broken into powder by using a crusher, and a standard sieve was used to screen the particles, between 20- and 40-mesh. The chemicals used in the test were the analytically reagents potassium hydroxide (KOH) and sodium hydroxide (NaOH). The elemental composition of CS was measured by an Elemental Analyzer (VARIO EL III) and proximate analysis was carried out in a muffle furnace (XH1L-14), as shown in Table 1.

**Table 1.** Elemental composition and industrial analysis of corn stalk.

| | **Ultimate Analysis (wt.%, Dry & Ash Free Basis)** | | | | | **Proximate Analysis (wt.%, Dry Basis)** | | |
|---|---|---|---|---|---|---|---|---|
| | **C** | **H** | **O** | **N** | **S** | **Volatile Matter** | **Fixed Carbon** | **Ash Content** |
| CS | 44.74 | 6.15 | 47.65 | 0.36 | 0.003 | 82.7 | 16.2 | 1.1 |

### *2.2. Preparation of AC*

According to the pyrolysis method for preparing AC, an appropriate amount of CS is first weighed and then placed in an alumina crucible located in a horizontal tube furnace (OTF-1200X, HF-Kejing, Hefei, China). Throughout the pyrolysis process, nitrogen is continuously injected into the tubular furnace at a flow rate of 200 mL/min to ensure that the reaction takes place in oxygen-free conditions. The pyrolysis process involved heating the sample from room temperature to 800 °C at a heating rate of 8 °C/min, and then holding

heat at this temperature for 120 min to promote the pyrolysis reaction of corn stalks to form pyrolytic carbon (CSBC).

The activated carbon was prepared using one-step and two-step methods, as given in Figure 1. One-step activation is carried out by uninterrupted carbonization activation in a tube furnace. The CS and an activating agent (KOH, NaOH and KOH/NaOH) were adequately mixed in a 1:1 mass ratio. Then, it is placed in a crucible. Before starting the reaction system, the tubular furnace was purged with nitrogen gas for 30 min to ensure that the carbonization and activation process took place under an inert atmosphere. Subsequently, the activation temperature was gradually increased from room temperature to the desired temperature (600, 700, and 800 °C, respectively) and maintained at that temperature for a certain time (60, 90, and 120 min, respectively). When the run is complete, nitrogen continues to be passed through the tube furnace to ensure anoxic conditions, and the product is removed after cooling to room temperature. Subsequently, the obtained activation products were soaked with 1 M HCl solution and then washed with deionized water to a pH of approximately 7. Finally, the one-step activated carbon was oven-dried at 100 °C for 3 h. One-step activated carbon is denoted as (I-activator-CSAC-activation temperature/activation time).

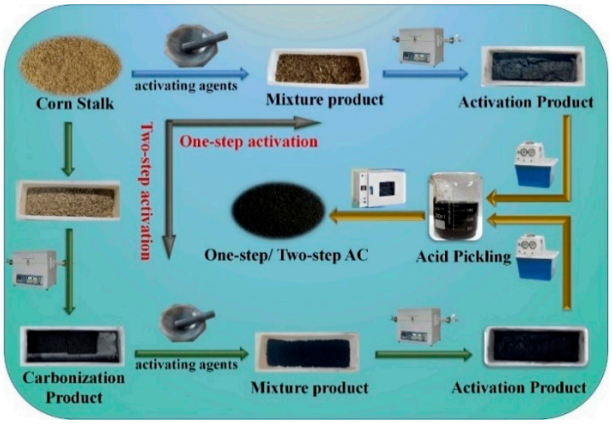


**Figure 1.** Experimental flowcharts for one-step and two-step preparation of AC.

In the two-step activation preparation process, a pre-carbonization stage was first carried out, and the sample was carbonized at 500 °C and maintained at that temperature for 120 min. Subsequently, the second activation stage was carried out, where the carbonized products were activated at 800 °C and maintained for 90 min. Except for the two key steps mentioned above, the rest of the entire two-step activation process is the same as the one-step method. The resulting two-step activated carbon was denoted as II-K-CSAC. The specific conditions for the preparation of AC are shown in Table 2.

**Table 2.** Preparation conditions of AC.

| Samples | Activating Agent | Activation Temperature (°C) | Activation Time (min) | Preparation Method |
|---|---|---|---|---|
| CSBC | / | 800 | 120 | pyrolysis |
| II-K-CSAC | KOH | 500/800 | 120/90 | Two-step |
| I-K-CSAC | KOH | 800 | 120 | one-step [a] |
| I-K-CSAC-600 | KOH | 600 | 120 | one-step |
| I-K-CSAC-700 | KOH | 700 | 120 | one-step |
| I-K-CSAC-800 | KOH | 800 | 120 | one-step |
| I-Na-CSAC | NaOH | 800 | 120 | one-step |
| I-K/Na-CSAC | KOH/NaOH | 800 | 120 | one-step |
| I-K-CSAC-60 | KOH | 800 | 60 | one-step |
| I-K-CSAC-90 | KOH | 800 | 90 | one-step |
| I-K-CSAC-120 | KOH | 800 | 120 | one-step |

[a.] If the activation temperature or activation time is not labeled in the one-step activated carbon, the default activation temperature is 800 °C and the activation time is 120 min.

### *2.3. Analytical Methods*

#### 2.3.1. Pyrolysis Characteristics of Biomass and AC

The combination of Thermogravimetry analysis (TG) and Derivative Thermogravimetry (DTG) was used to investigate the pyrolysis process of biomass and mixed feedstocks (CS/KOH) as well as activated carbon. In each experiment, a 10 mg sample was placed in a crucible. Nitrogen (purity ≥ 99.999%) was used to purge for 30 min before starting the reaction system to ensure that the entire reaction process was in an inert atmosphere. The temperature was increased from 30 °C to 950 °C in an atmosphere of nitrogen (flow rate 50 mL/min) at a heating rate of 10 °C/min.

#### 2.3.2. Characterization of AC

Fourier-Transform Infrared Spectroscopy (FTIR, Tensor 27, Bruker, Berlin, Germany) was utilized to determine the type of functional groups present in AC in the range of 4000–400 $cm^{-1}$ by the KBr pellet method. The crystal structure of the AC was characterized using X-ray diffraction (XRD, D8 Advance A25, Bruker, Berlin, Germany) with a scan range from 10 to 70°. The surface morphology and structure of AC were characterized using scanning electron microscopy (SEM, SU8220, Hitachi, Tokyo Japan). The $N_2$ adsorption–desorption isotherm of activated carbon at 77 K was determined by a surface area analyzer (ASAP 2460, Micromeritics, Norcross, USA) and the specific surface area was calculated using the Brunauer–Emmett–Teller (BET) method. The electrochemical properties of AC were tested at the electrochemical workstation (CHI660E, Chenhua, Beijing, China).

## 3. Results and Discussion

### *3.1. Thermal Decomposition Properties of Biomass and AC*

#### 3.1.1. Thermal Decomposition Properties of Biomass

The thermal decomposition process of biomass with (CS/KOH) and without (CS) activating agent was investigated to demonstrate the effect of activating agent on biomass pyrolysis. The thermal decomposition processes of CS and CS/KOH are shown in Figure 2. The TG curve (Figure 2a) observes that the biomass undergoes three major stages of decomposition. When the temperature is below 120 °C, this is referred to as the pre-pyrolysis stage. In this stage, water molecules are removed from the biomass, and light volatiles are evaporated [26]. At the same time, the DTG curve (Figure 2b) appears as the peak of the first one. The second stage (120–500 °C) was mainly due to the thermal decomposition of the biomass components. The DTG curve exhibits a prominent peak corresponding to the decomposition of cellulose and hemicellulose [27]. However, comparing the TG curves of CS/KOH and CS, clearly shows that the mass loss of CS/KOH is significantly higher than that of CS in the temperature range below 320 °C. This is due to the fact that in this stage, the biomass undergoes a dehydration reaction to produce $K_2O$ (Equation (1)), and then water vapor reacts with the carbon to produce CO and $H_2$ (Equation (2)), which in turn produces more $CO_2$ (Equation (3)). The third stage is the decomposition process of lignin. At temperatures above 500 °C, lignin decomposes at a slow rate [28]. In this stage, the mass loss of CS/KOH is low relative to CS due to the reaction of KOH with $CO_2$ to form $K_2CO_3$ (Equation (4)) [29]. Finally, under high-temperature conditions, the TG and DTG curves of CS and CS/KOH tend to stabilize, indicating that the biomass pyrolysis reaction has been completed.

$$KOH \rightarrow K_2O + H_2O \quad (1)$$

$$C + H_2O \rightarrow CO + H_2 \quad (2)$$

$$CO+H_2O \rightarrow CO_2 + H_2 \quad (3)$$

$$CO_2 + K_2O \rightarrow K_2CO_3 \quad (4)$$

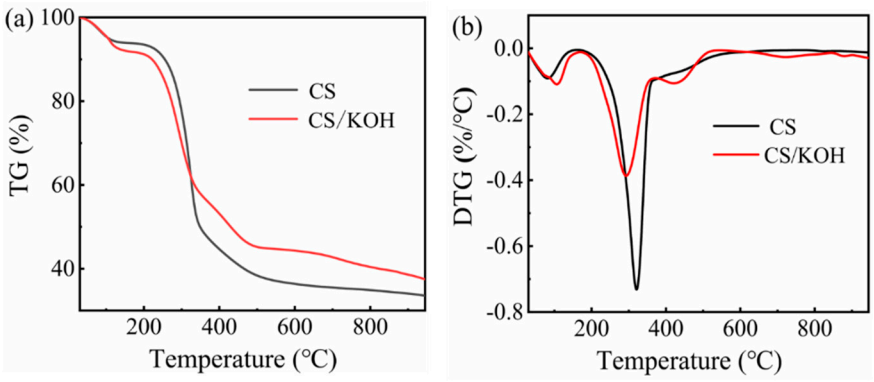


**Figure 2.** Thermal decomposition characteristics of CS and CS/KOH: (**a**) TG curve, (**b**) DTG curve.

#### 3.1.2. Thermal Decomposition Properties of AC

The effect of the preparation method on the activated carbon pyrolysis was demonstrated by studying the thermal decomposition behavior of activated carbon under different preparation methods, as shown in Figure 3. The weight loss rates for CSBC, I-K-CSAC, and II-K-CSAC were 15%, 13.1%, and 9.6%, respectively, throughout the thermal decomposition process. The final weight of the AC residue shows that the three ACs had different thermal stability: I-K-CSAC has excellent thermal stability, while CSAC has the worst thermal stability [30].

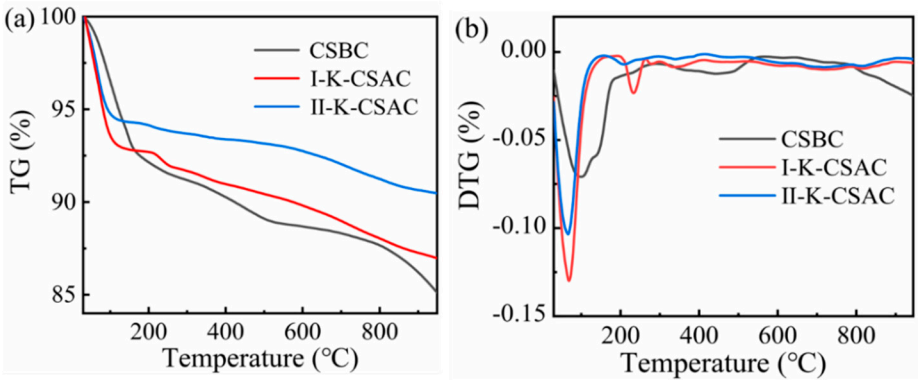


**Figure 3.** Thermal decomposition characteristics of CSBC, I-K-CSAC, and II-K-CSAC: (**a**) TG curve, (**b**) DTG curve.

### *3.2. Effect of Preparation Method on Properties of AC*

#### 3.2.1. FTIR Analysis

The FTIR spectra of AC acquired from different preparation methods are given in Figure 4. As can be seen, all the activated carbons (ACs) exhibit similar surface functional groups. The peak at 3435 $cm^{-1}$ belongs to the stretching vibration of the hydroxyl (–OH) group, signifying the existence of hydroxyl groups or water molecules on the AC surface [31,32]. Additionally, the absorption peaks at 2920 $cm^{-1}$ and 2850 $cm^{-1}$ can be attributed to the C–H stretching vibrations of alkanes. The peak observed at 1630 $cm^{-1}$ represents the stretching vibration of C=C double bonds in the aromatic ring. Furthermore, the absorption peaks at 1430 $cm^{-1}$ and 1049 $cm^{-1}$ correspond to the asymmetric stretching vibrations of the –CH and C–O groups. It can be inferred that the ACs obtained from different preparation methods contain oxygen-containing functional groups such as carbonyl, hydroxyl,

ester, and ether groups. However, I-K-CSAC has a stronger absorption peak intensity compared to II-K-CSAC. This difference can be attributed to the two-step method, resulting in a more thorough decomposition of the organic functional groups present in II-K-CSAC.

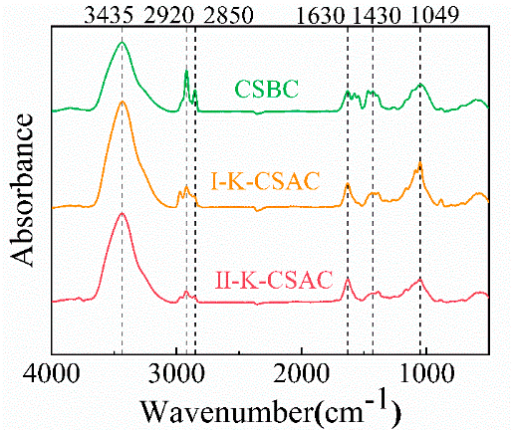


**Figure 4.** FTIR spectra of CSBC, I-K-CSAC, and II-K-CSAC.

3.2.2. XRD Analysis

Figure 5 presents the XRD patterns of AC obtained by different preparation methods ranging from 10 to 70°. Through the analysis of XRD pattern, the crystal structure and crystal plane properties of AC can be understood. The XRD patterns of AC showed broader diffraction peaks at 18–28° and 41–45°, corresponding to the graphite structure (002) and (100) crystallographic planes [33]. The presence of these peaks indicates the presence of a crystalline portion of the graphite structure in the activated carbon. Specifically, the (002) crystallographic plane consists of successive layers of parallel graphite flakes, while the (100) crystal plane reflects the size of the aromatic microcrystals in a single plane [34]. In addition, more diffraction peaks were observed in the XRD pattern of CSBC, which corresponded to the diffraction peaks of KCl at 28.3°, 40.5° and 47.9°, and the diffraction peaks of $SiO_2$ at 26.3°. However, the XRD patterns of I-K-CSAC and II-K-CSAC doing not show obvious miscellaneous peaks. This indicates that during the preparation process, the biomass reacts strongly with the activating agent, resulting in the removal or rearrangement of minerals in the biomass and the formation of an amorphous structure. According to the intensity of peaks, the intensity of graphite structure peaks in the XRD spectra of II-K-CSAC was significantly higher than that of I-K-CSAC. This indicates that the two-step activation process enhances the graphite structure of II-K-CSAC and makes it have more obvious graphite crystal properties.

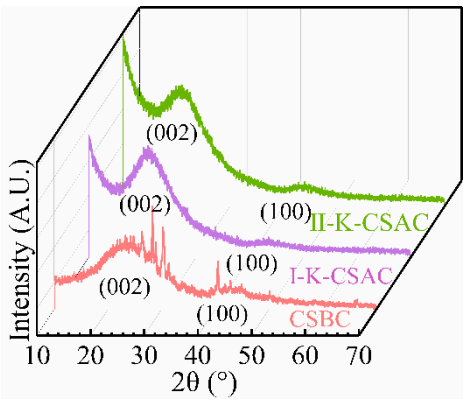


**Figure 5.** XRD patterns of CSBC, I-K-CSAC, and II-K-CSAC.

3.2.3. SEM and $N_2$ Adsorption-Desorption Analysis

The study of the structure of AC is helpful for revealing the pore structure of AC in various induced conditions. SEM images of AC using different preparation methods are presented in Figure 6. The surface of CSBC is smooth with no obvious pore structure. In contrast, I-K-CSAC exhibits an abundant pore structure like a honeycomb structure, which is in sharp contrast to CSBC. This result confirms that KOH activation promotes the transformation of non-porous to abundantly porous structures [35]. On the other hand, II-K-CSAC exhibits tubular structures that extends into the interior, indicating that different activation processes led to significant differences in the surface morphology of AC.

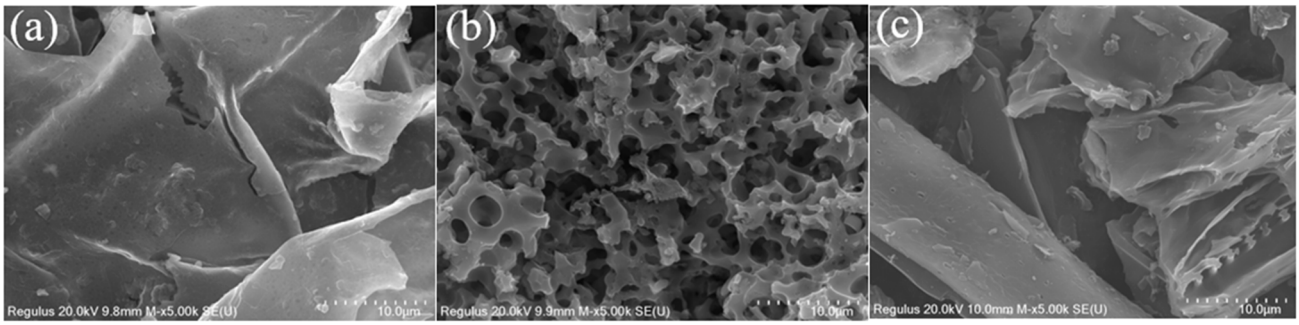


**Figure 6.** SEM images of (**a**) CSBC, (**b**) I-K-CSAC, and (**c**) II-K-CSAC.

By observing the SEM results, it can be seen that the pore structure of AC is quite different with different preparation methods. Therefore, the pore structure characteristics of activated carbon were further characterized. The $N_2$ adsorption–resolution isotherm test and pore size distribution of the three ACs are shown in Figure 7. Due to the very poor adsorption capacity of CSBC, it was shown that pyrolytic charcoal does not possess a porous structure. According to the IUPAC classification, the adsorption amount of I-K-CSAC rose rapidly at lower relative pressure, which is consistent with the isothermal property of type I(b), indicating that I-K-CSAC has an abundant mesoporous structure. In contrast, the adsorption–desorption isotherm of II-K-CSAC belonged to type IV, and capillary condensation occurred in the adsorbent at $p/p_0 > 0.3$ with an obvious H4-type hysteresis loop, reflecting that the adsorbent had a narrow mesoporous fracture. By observing the pore size distribution in Figure 7b, it can be found that the mesoporous structures of I-K-CSAC and II-K-CSAC are mainly distributed in the range of 2.0~10 nm. The specific surface area obtained by BET method and the total pore volume obtained from BJH method are shown in Table 3. Compared with CSBC ($S_{BET}$ = 9.676 $m^2/g$, $V_{Total}$ = 0.0254 $cm^3/g$) and II-K-CSAC ($S_{BET}$ = 860 $m^2/g$, $V_{Total}$ = 0.3009 $cm^3/g$), I-K-CSAC had the highest BET surface area (1725 $m^2/g$) and the largest total pore volume (0.7497 $cm^3/g$). Meanwhile, a comparison of the results of in this study with those of previous researchers shows that AC prepared by one-step activation in the present study has a higher specific surface area under similar conditions.

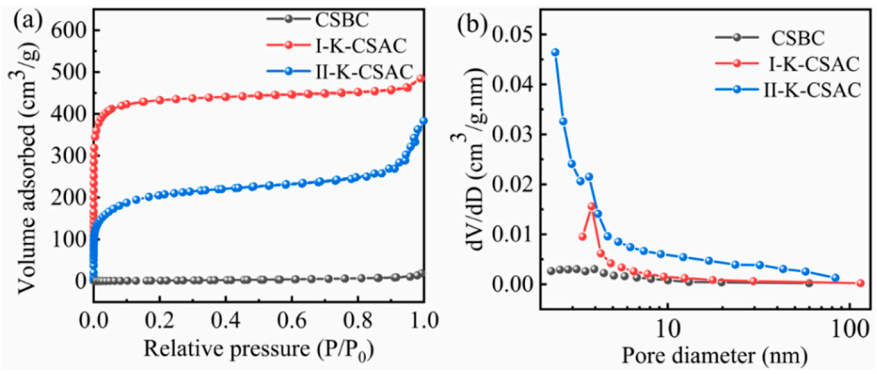

**Figure 7.** $N_2$ adsorption/desorption isotherms (**a**) and pore size distributions (**b**) of CSBC, I-K-CSAC and II-K-CSAC.

**Table 3.** Comparison of pore texture characteristics and $S_{BET}$ of ACs.

| Raw Material/Samples | Activating Agent | Activation Temperature (°C) | Activation Time (min) | $S_{BET}$ ($m^2/g$) | $V_{Total}$ ($cm^3/g$) | Reference |
|---|---|---|---|---|---|---|
| CSBC | / | 800 | 120 | 9.676 | 0.0254 | |
| I-K-CSAC | KOH | 800 | 120 | 1725 | 0.7497 | This study |
| II-K-CSAC | KOH | 500/800 | 120/90 | 860 | 0.3009 | |
| Mangosteen peel | KOH | 800 | 120 | 1039 | 0.635 | [36] |
| Phyllostachys edulis | KOH | 800 | 60 | 1123 | 0.4478 | [37] |

3.2.4. Electrochemical Properties Analysis

Figure 8 demonstrates the electrochemical property of CSBC, I-K-CSAC, and II-K-CSAC by CV curves at various scanning rates. The range of scanning rate is from 20 mV/s to 220 mV/s with the equal rate interval of 20 mV/s. At the scan rate increases, the peak response current of the AC increases. As a scan rate of 220 mV/s, the CSBC has a weak peak current response. Its peak anodic current ($I_{pa}$) and peak cathodic current ($I_{pc}$) were 114.2 μA and −114.9 μA, respectively. This indicates that the electrochemical property of CSBC is unsatisfactory. The CV curve of I-K-CSAC showed a very high peak current response: its peak anodic current ($I_{pa}$) and peak cathodic current ($I_{pc}$) were 159.8 μA and −169.5 μA, respectively. This shows that I-K-CSAC has excellent electrochemical properties. This excellent electrochemical performance is closely associated with the honeycomb porous structure of I-K-CSAC. The porous structure of the carbon material not only enhances its adsorption capacity but also offers ample space for the adsorption of electrolytic ions. [38]. The CV curves of II-K-CSAC showed a slightly lower peak current response ($I_{pa}$ = 130.8 μA, $I_{pc}$ = −129.9 μA), which was strongly related to the preparation method of the activated carbon [39].

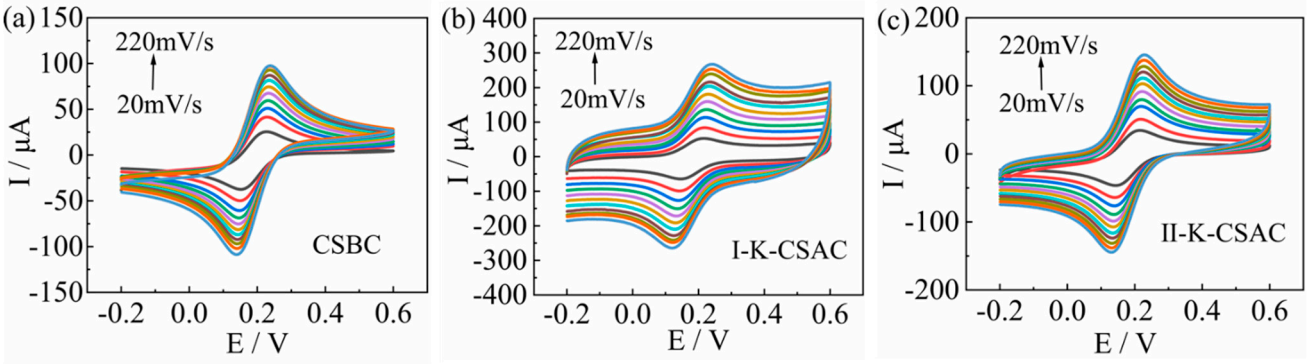


**Figure 8.** CV curves of (**a**) CSBC, (**b**) I-K-CSAC, and (**c**) II-K-CSAC.

*3.3. Effect of Preparation Temperature on the Properties of AC*

The physicochemical characteristics of AC prepared using various methods were analyzed. The results revealed that the one-step method yielded AC with superior physicochemical characteristics compared to the pyrolysis and two-step methods. In the further study, AC was prepared by a one-step activation method, and the effect of activation temperature on AC properties was studied.

3.3.1. FTIR Analysis

The FTIR spectra of AC prepared at different activation temperatures are presented in Figure 9. It is noteworthy that when the activation temperature was increased to 800 °C, the intensity of the absorption peaks were significantly weakened, particularly the C–

O absorption peaks. This phenomenon suggests that high temperature helps intensify the activation reactions, leading to the volatilization and decomposition of certain functional groups [40]. Furthermore, the ACs labeled as I-CSAC-600, I-CSAC-700, and I-CSAC-800 exhibit the existence of similar functional groups, for example –OH, C–H, C=C, –CH, and C–O. These findings suggest that ACs activated at different temperatures (600, 700, and 800 °C) possess similar chemical compositions and structures.

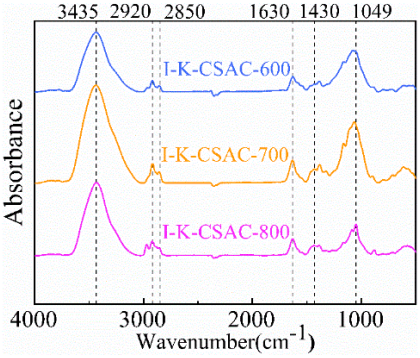


**Figure 9.** FTIR spectra of I-CSAC-600, I-CSAC-700, and I-CSAC-800.

### 3.3.2. XRD Analysis

The XRD patterns of AC obtained in various activation temperatures are given in Figure 10. The absence of distinct sharp diffraction peaks in the XRD patterns of the three ACs suggests that they were weakly crystalline [41]. The broad peaks at 21° and 43° correspond to the (002) and (100) crystal planes of the graphite layer, respectively. The presence of (002) crystal plane points to the existence of parallel stacking and interconnection between some graphite flakes in the AC [42]. The (100) crystal plane indicates that the $sp^2$ hybridized carbon atoms in the AC interacted to form a hexagonal lattice structure. Moreover, the AC was activated to move toward an ordered carbon structure. In addition, the XRD patterns of I-CSAC-600, I-CSAC-700, and I-CSAC-800 were not markedly different, which suggests that the activation temperatures (600, 700, and 800 °C) had little effect on the composition and amorphous carbon structure of AC.

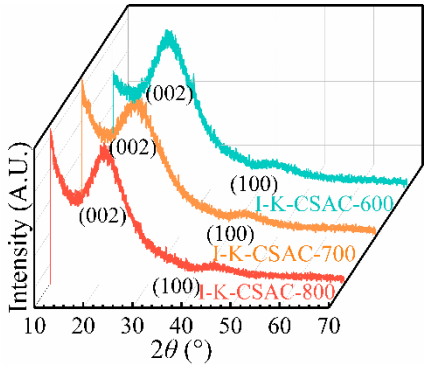


**Figure 10.** XRD patterns of I-CSAC-600, I-CSAC-700, and I-CSAC-800.

### 3.3.3. SEM Analysis

The surface morphology of AC gained at different activation temperatures is presented in Figure 11. The AC produced at diverse activation temperatures exhibited significant porous structures. For I-CSAC-600, the surface exhibited an irregular pore structure. Although the material exhibited a rich pore structure, there were some visible partially closed or incompletely opened pores. Unlike I-CSAC-600, the I-K-CSAC-700 displayed a three-dimensional skeleton structure with an increase in pore size. As the activation temperature increased to 800 °C, the pore structure of I-K-CSAC-800 became denser,

indicating that high-temperature activation is conducive to the formation of a richer pore structure on the surface of AC. However, small particles appeared on the surface of I-K-CSAC-800, implying that the pore structure became unstable due to high temperature.

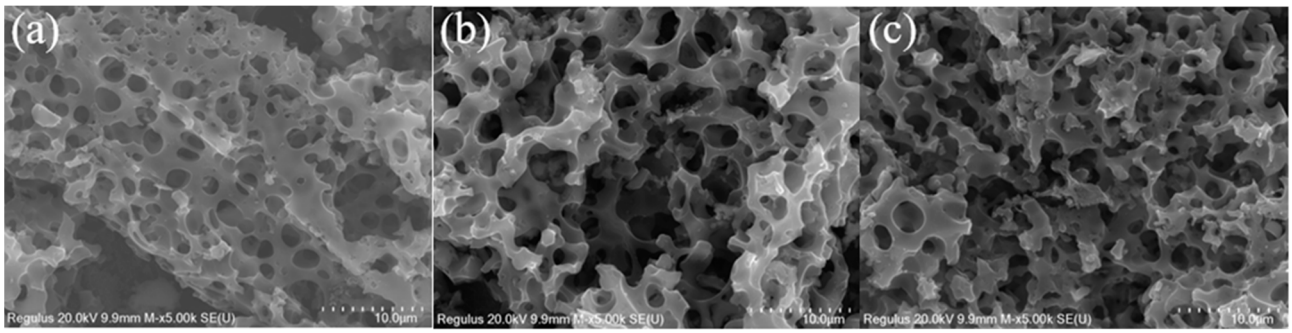


**Figure 11.** SEM images of (**a**) I-K-CSAC-600, (**b**) I-K-CSAC-700, and (**c**) I-K-CSAC-800.

3.3.4. Electrochemical Properties Analysis

Figure 12 demonstrates the CV curves of AC prepared at various activation temperatures. The CV curves present the peak current response of I-CSAC-600, I-CSAC-700, and I-CSAC-800. When the scan rate was 220 mV/s, the anodic peak currents ($I_{pa}$) of CSAC-600, I-CSAC-700, and I-CSAC-800 were 111.6 μA, 123.3 μA, and 159.8 μA, respectively. The cathodic peak currents ($I_{pc}$) were −110.7 μA, −123.5 μA, and −169.5 μA, respectively. The peak current response of AC increased with increasing activation temperatures (600, 700, and 800 °C), and the electrochemical performance of AC also increased. This phenomenon was due to the rich porous structure of AC as the activation temperature increases. The porous structure creates an ideal surface environment for ion diffusion during charging and discharging, thus improving the electrochemical performance of AC.

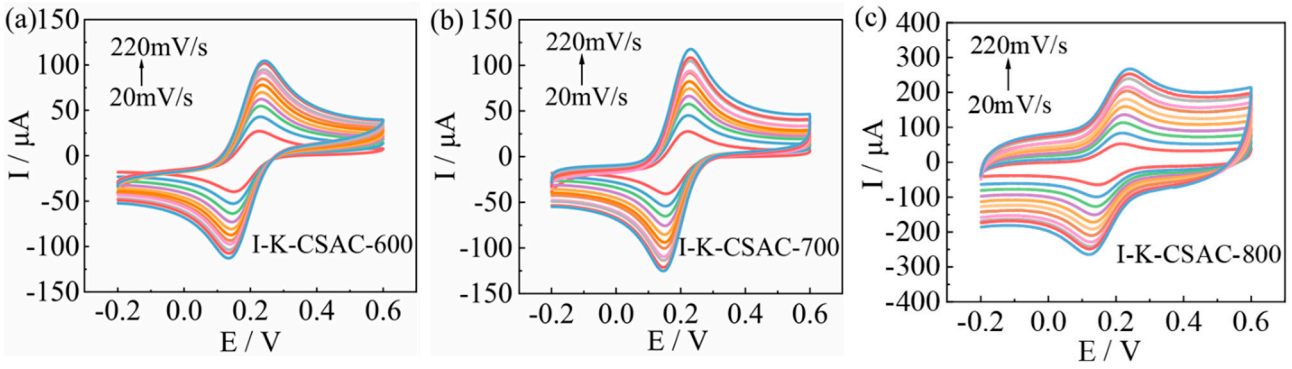


**Figure 12.** CV curves of (**a**) I-K-CSAC-600, (**b**) I-K-CSAC-700, and (**c**) I-K-CSAC-800.

*3.4. Effect of Activating Agent on the Properties of AC*

3.4.1. FTIR Analysis

Molten salt, as the activating agent, undergoes liquefaction at low temperatures. Molten salts in ionic form penetrate more easily into the biomass structure and break the hydrogen bonds between molecules, thus contributing to biomass cracking. It is worth noting that different types of molten salts used can also lead to changes in the physicochemical properties of the final AC. The FTIR spectra of AC prepared with different activating agents are shown in Figure 13. I-K-CSAC, I-Na-CSAC, and I-K/Na-CSAC have similar functional groups. The intensity of the absorption peaks of I-K-CSAC is slightly higher than that of I-Na-CSAC, especially the stretching vibration peak of -OH near 3440 $cm^{-1}$ and the stretching vibration peak of C–O near 1049 $cm^{-1}$. This discrepancy can be attributed to the higher activation and intercalation ability of KOH compared to NaOH at elevated temperatures. During the activation process, KOH not only reacts with the

surface of the raw materials but also infiltrates the irregular graphite layers and reacts with the inner carbon, thereby introducing more oxygen-containing functional groups. Compared with the single activating agent, the intensity of C–H and C–O absorption peaks in I-K/Na-CSAC was significantly enhanced, indicating that the combined action of KOH and NaOH could introduce more functional groups and further improve the properties of AC.

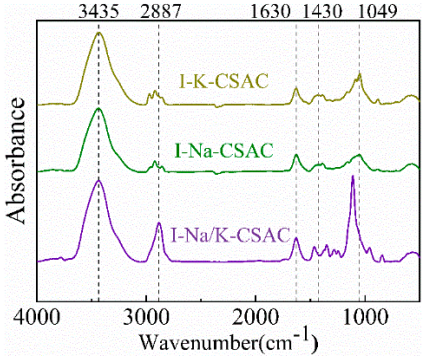


**Figure 13.** FTIR spectra of I-K-CSAC, I-Na-CSAC, and I-K/Na-CSAC.

3.4.2. XRD Analysis

The XRD patterns of AC prepared with various activating agents are given in Figure 14. The X-ray patterns of I-K-CSAC, I-Na-CSAC, and I-K/Na-CSAC showed (002) and (100) crystal peaks [34]. Moreover, no sharp diffraction peaks appeared, which indicated that the AC had an amorphous structure after activation by the activating agent.

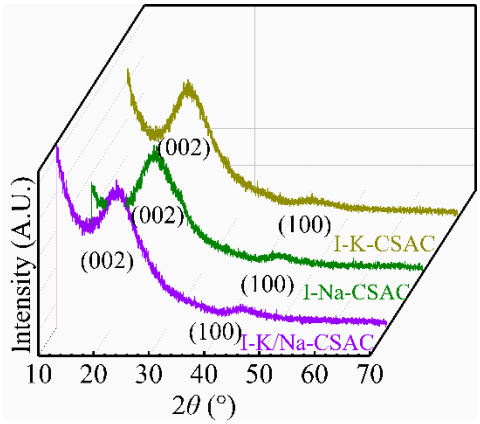


**Figure 14.** XRD patterns of I-K-CSAC, I-Na-CSAC, and I-K/Na-CSAC.

3.4.3. SEM Analysis

Figure 15 demonstrates the SEM images of AC with different activating agents. It can be observed that the surface of I-K-CSAC has an abundant pore structure with dense pores and different pore diameters. The pore structure of I-Na-CSAC is more complex, and the surface of the carbon skeleton structure becomes rough and loosely organized. Under the joint action of activating agents KOH and NaOH, I-K/Na-CSAC became more fragmented. Notably, the I-K-CSAC pore structure is the most developed. This is attributed to the interaction of potassium metal with the internal structure of the carbon lattice, which enlarges the space of the aromatic layer of AC and induces distortion of the carbon layer, leading to the formation of a rich pore structure [42]. Furthermore, the role of metal potassium vapors is unique and critical for the formation of a well-developed pore structure.

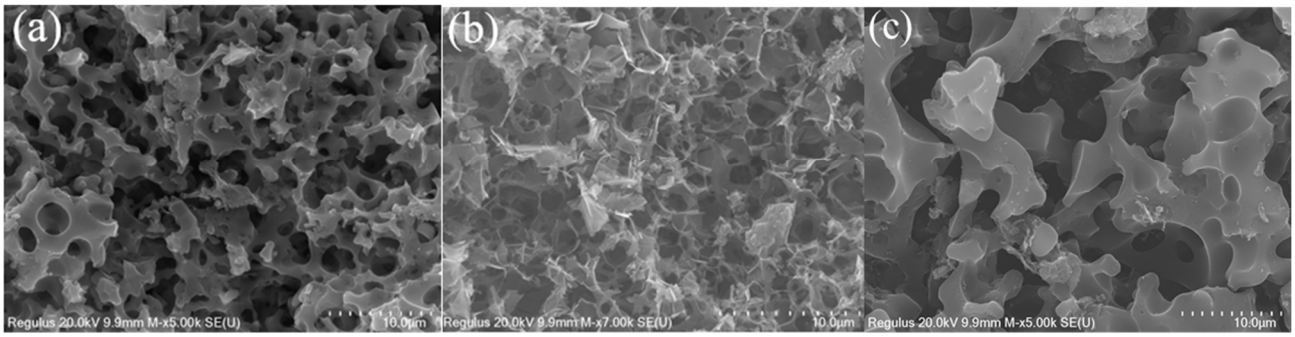


**Figure 15.** SEM images of (**a**) I-K-CSAC, (**b**) I-Na-CSAC, and (**c**) I-K/Na-CSAC.

3.4.4. Electrochemical Properties Analysis

The CV curves of I-K-CSAC, I-Na-CSAC, and I-K/Na-CSAC are shown in Figure 16. The peak current response of I-K-CSAC presents a very satisfactory electrochemical property. At the scan rate of 220 mV/s, the anodic peak current ($I_{pa}$) and cathodic peak current ($I_{pc}$) were 159.8 μA and −169.5 μA, respectively. Meanwhile, I-Na-CSAC also has a relatively good peak current response ($I_{pa}$ = 157.7 μA, $I_{pc}$ = −150.5 μA). For I-K/Na-CSAC, the peak response current is somewhat reduced. It is shown that the electrochemical properties of AC do not improve with the increase in the activating agent type. Compared with I-Na-CSAC and I-K/Na-CSAC, I-K-CSAC has higher electrochemical properties. This may be attributed to the fact that the potassium metal in KOH alters the distribution of the electron cloud of carbon atoms around the aromatic layer, resulting in more reactive active sites, which leads to an increase in the electrochemical performance of AC [43].

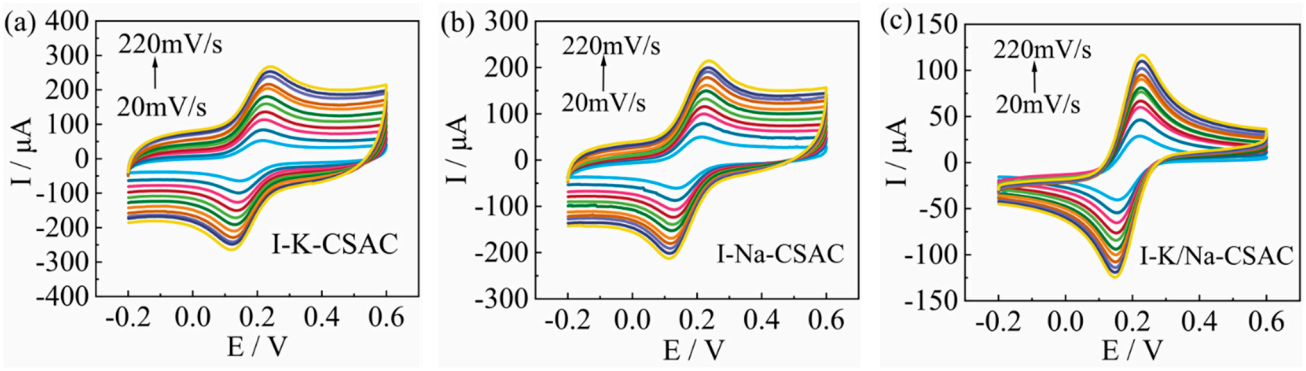


**Figure 16.** CV curves of (**a**) I-K-CSAC, (**b**) I-Na-CSAC, and (**c**) I-K/Na-CSAC.

*3.5. Effect of Activation Time on the Properties of AC*

3.5.1. FTIR Analysis

The FTIR spectra of AC prepared at different activation times are shown in Figure 17. It can be observed that the intensity of absorption peaks and functional group types of I-K-CSAC-90 and I-K-CSAC-60 are basically the same. However, the absorption peak intensity and functional group type of I-K-CSAC-120 were significantly weakened in comparison. This weakening may be attributed to the longer activation reaction time of I-K-CSAC-120, which allowed the organic matter in the biomass to be fully decomposed and volatilized.

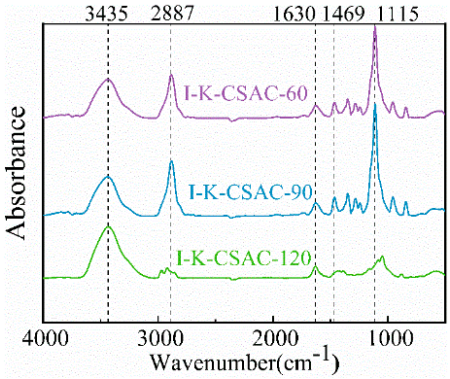


**Figure 17.** FTIR spectra of I-K-CSAC-60, I-K-CSAC-90, and I-K-CSAC-120.

### 3.5.2. XRD Analysis

The results of the physical structure characterization of AC with different activation times using XRD are shown in Figure 18. The XRD pattern showed that the AC contained (002) and (100) crystal peaks and the intensity of the crystal peaks are essentially the same [34]. However, the X-ray pattern of I-K-CSAC-60 showed sharp diffraction peaks, while the X-ray patterns of I-K-CSAC-90 and I-K-CSAC-120 did not. This observation may suggest that as the activation time increases, the KOH reacts sufficiently with the biomass, causing the inorganic matter in the biomass to form soluble compounds. After acid washing, these soluble compounds were removed, resulting in the absence of visible crystal diffraction peaks in AC.

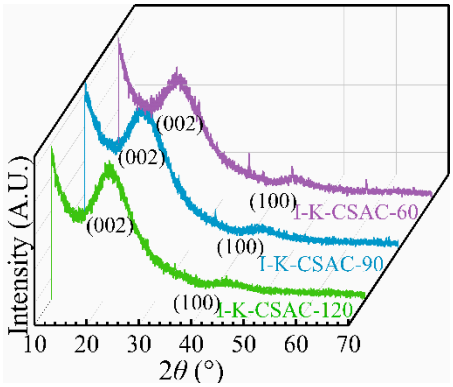


**Figure 18.** XRD patterns of I-K-CSAC-60, I-K-CSAC-90, and I-K-CSAC-120.

### 3.5.3. SEM Analysis

Figure 19 provides SEM images of AC prepared from different activation times. There is no remarkable discrepancy between the surface morphology of I-K-CSAC-60 and I-K-CSAC-90, and a certain number of pore structures appeared on the surface of AC. In contrast, the I-K-CSAC-120 tissue structure showed more small pores and channels with abundant pore structure. This suggests that adequate activation time facilitates the full reaction between KOH and biomass to form a well-developed pore structure.

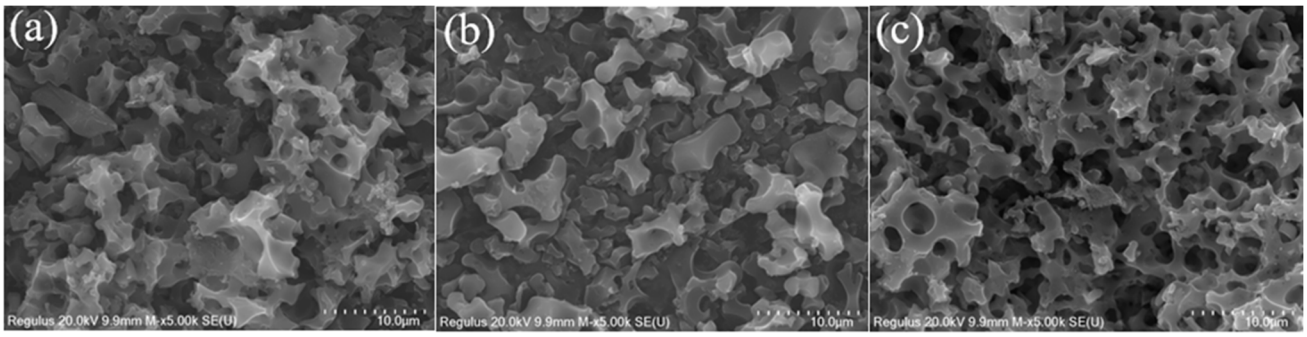


**Figure 19.** SEM images of (**a**) I-K-CSAC-60, (**b**) I-K-CSAC-90, and (**c**) I-K-CSAC-120.

3.5.4. Electrochemical Properties Analysis

The CV curves of AC at various activation times are presented in Figure 20. I-K-CSAC-60 and I-K-CSAC-90 exhibited similar CV curves, both showing relatively weak peak current responses. At a scan rate of 220 mV/s, the anodic peak current ($I_{pa}$) and cathodic peak current ($I_{pc}$) of I-K-CSAC-60 were 129.4 μA and −126.2 μA, respectively. Similarly, the anodic peak current ($I_{pa}$) and cathodic peak current ($I_{pc}$) of I-K-CSAC-90 were 130.7 μA and −128.8 μA, respectively. Notably, as illustrated in Figure 20c, I-K-CSAC-120 demonstrated a higher peak current response ($I_{pa}$ = 159.8 μA, $I_{pc}$ = −169.5 μA). The significant improvement in electrochemical performance was mainly due to the extension of activation time, which made the activating agent react more fully with the biomass, formed a more developed pore structure and more ion channels, and significantly improved the transport efficiency of electrolyte ions.

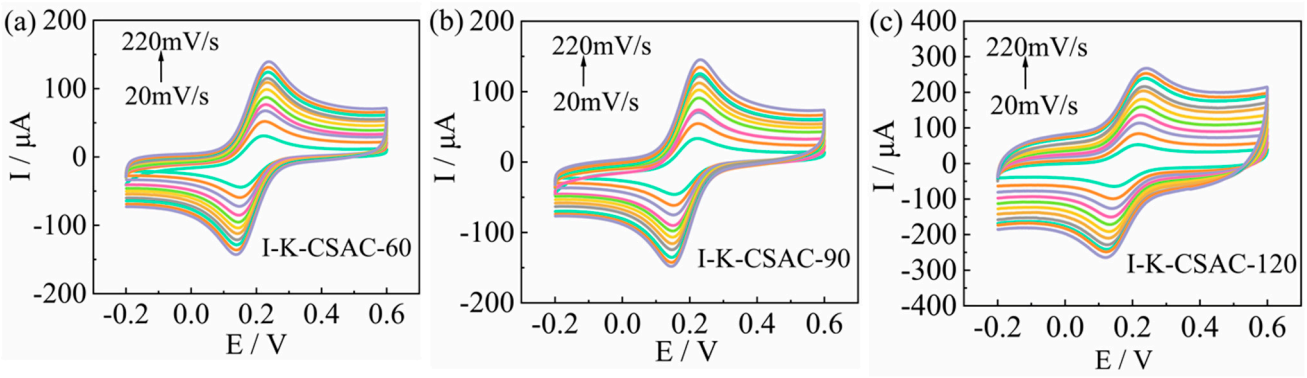


**Figure 20.** CV curves of (**a**) I-K-CSAC-60, (**b**) I-K-CSAC-90, and (**c**) I-K-CSAC-120.

## 4. Conclusions

In this study, activated carbon (AC) was prepared from corn stalk by pyrolysis, one-step activation and two-step activation. Subsequently, a single-factor experiment was carried out to investigate the preparation of porous AC under different conditions of temperature, activating agent and activation time, and the effects of these conditions on the physicochemical properties of AC were studied. It was shown that the AC obtained from one-step activation exhibited abundant spongy porous structure and excellent electrochemical properties compared with those prepared by pyrolysis and two-step activation. Basis on the one-step activation, the optimal activation conditions were determined: an activation temperature of 800 °C, activating agent of KOH, and activation time of 120 min. In this study, a set of optimal process parameters were successfully determined. By carefully regulating these parameters, the activated carbon obtained has abundant pore structure and excellent electrochemical properties. These optimized process parameters provide important guidance for the preparation of activated carbon, so that it can show excellent performance in adsorption, energy storage and other fields.

**Author Contributions:** B.X.: formal analysis, investigation, methodology, visualization, and writing—original draft preparation; M.C.: investigation, validation; C.F.: formal analysis, methodology; J.H.: data curation; Y.W.: resources; Y.F.: conceptualization, resources, supervision, and writing—review and editing; Z.Z.: supervision. All authors have read and agreed to the published version of the manuscript. All authors have read and agreed to the published version of the manuscript.

**Funding:** This work was supported by the National Key Research and Development Program in China (Y.F., Grant No. 2018YFE0206600), Scientific and Technological Research Projects of Henan Province (Y.W., Grant No. 232102240093).

**Institutional Review Board Statement:** Not applicable.

**Data Availability Statement:** All data generated for this study are presented within the manuscript.

**Conflicts of Interest:** The authors declare that they have no known competing financial interest or personal relationships that could have appeared to influence the work reported in this paper.

## References

1. Hu, L.; Wei, X.; Guo, X.; Lv, H.; Wang, G. Investigation on the kinetic behavior, thermodynamic and volatile products analysis of chili straw waste pyrolysis. *J. Environ. Chem. Eng.* **2021**, *9*, 105859. https://doi.org/10.1016/j.jece.2021.105859.
2. McLaughlin, L.P.; Belmont, E.L. Size-resolved aerosol emissions from lignocellulosic biomass and biomass constituent pyrolysis under variable dilution temperatures. *J. Aerosol Sci.* **2021**, *151*, 105679. https://doi.org/10.1016/j.jaerosci.2020.105679.
3. Egun, I.L.; He, H.; Hu, D.; Chen, G.Z.; Molten Salt Carbonization and Activation of Biomass to Functional Biocarbon. *Adv. Sustain. Syst.* **2022**, *6*, 2200294. https://doi.org/10.1002/adsu.202200294.
4. Isahak, W.N.R.W.; Hisham, M.W.M.; Yarmo, M.A. Highly porous carbon materials from biomass by chemical and carbonization method: A comparison study. *J. Chem.* **2012**, *2013*, 620346. https://doi.org/10.1155/2013/620346.
5. Barjasteh-Askari, F.; Davoudi, M.; Dolatabadi, M.; Ahmadzadeh. S. Iron-modified activated carbon derived from agro-waste for enhanced dye removal from aqueous solutions. *Heliyon* **2021**, *7*, e07191. https://doi.org/10.1016/j.heliyon.
6. Lobato-Peralta, D.R.; Amaro, R.; Arias, D.M.; Cuentas-Gallegos, A.K.; Jaramillo-Quintero, O. A.; Sebastian, P.J.; Okoye, P.U. Activated carbon from wasp hive for aqueous electrolyte supercapacitor application. Electroanalytical. Chem. 2021, 901, 115777.
7. Liao, W.; Zhang, X.; Ke, S.; Shao, J.; Yang, H.; Zhang, S.; Chen, H. Effect of different biomass species and pyrolysis temperatures on heavy metal adsorption, stability and economy of biochar. *Ind. Crop. Prod.* **2022**, *186*, 115238. https://doi.org/10.1016/j.indcrop.2022.115238.
8. Cai, Z.Z.; Liu, Q.; Li, H.X.; Wang, J.Y.; Tai, G.Y.; Wang, F.; Han, J.G.; Zhu, Y.L.; Wu, G.Y. Waste-to-resource strategy to fabricate functionalized MOFs composite material based on durian shell biomass carbon fiber and $Fe_3O_4$ for highly efficient and recyclable dye adsorption. *Int. J. Mol. Sci.* **2022**, *23*, 5900. https://doi.org/10.3390/ijms23115900.
9. Anuar, N.F.; Shah, D.R.S.I.; Ramli, F.F.; Zaini, M.S.M.; Mohammadi, N.A.; Daud, A.R.M.; Syed-Hassan, S.S.A. The removal of antibiotics in water by chemically modified carbonaceous adsorbents from biomass: A systematic review. *J. Clean. Prod.* **2023**, *401*, 136725. https://doi.org/10.1016/j.jclepro.2023.136725.
10. Luo, L.; Lan, Y.L.; Zhang, Q.Q.; Deng, J.P.; Luo, L.C.; Zeng, Q.Z.; Gao, H.L.; Zhao, W.G. A review on biomass-derived activated carbon as electrode materials for energy storage supercapacitors. *J. Energy Storage* **2022**, *55*, 105839. https://doi.org/10.1016/j.est.2022.105839.
11. Murali, G.; Harish, S.; Ponnusamy, S.; Ragupathi, J.; Therese, H.A.; Navaneethan, M.; Muthamizhchelvan, C. Hierarchically porous structured carbon derived from peanut shell as an enhanced high rate anode for lithium ion batteries. *Appl. Surf. Sci.* **2019**, *492*, 464–472. https://doi.org/10.1016/j.apsusc.2019.06.142.
12. Zainal, N.H.; Aziz, A.A.; Idris, J.; Jalani, N.F.; Mamat, R.; Ibrahim, M.F.; Hassan, M.A.; Abd-Aziz, S. Reduction of POME final discharge residual using activated bioadsorbent from oil palm kernel shell. *J. Clean. Prod.* **2018**, *182*, 830–837. https://doi.org/10.1016/j.jclepro.2018.02.110.
13. Mortada, W.I.; Mohamed, R.A.; Monem, A.A.A.; Awad, M.M.; Hassan, A.F. Effective and low-cost adsorption procedure for removing chemical oxygen demand from wastewater using chemically activated carbon derived from rice husk. *Separations* **2023**, *10*, 43. https://doi.org/10.3390/separations10010043.
14. Eda, K.; Canan, A.B. Preparation, structural evaluation and adsorptive properties of activated carbon from agricultural waste biomass. *Adv. Powder Technol.* **2015**, *26*, 811–818. https://doi.org/10.1016/j.apt.2015.02.006.
15. Dang, H.; Xu, R.S.; Zhang, J.L.; Wang, M.Y.; Ye, L.; Jia, G.L. Removal of oxygen-containing functional groups during hydrothermal carbonization of biomass: Experimental and DFT study. *Energy* **2023**, *276*, 127436. https://doi.org/10.1016/j.energy.2023.127436.
16. Ahmed, M.J.; Theydan, S.K. Adsorption of cephalexin onto activated carbons from Albizia lebbeck seed pods by microwave-induced KOH and $K_2CO_3$ activations. *Chem. Eng. J.* **2012**, *211–212*, 200–207. https://doi.org/10.1016/j.cej.2012.09.089.
17. Zhang, W.; Cheng, R.R.; Bi, H.H.; Lu, Y.H.; Ma, L.B.; He, X.J. A review of porous carbons produced by template methods for supercapacitor applications. *New Carbon Mater.* **2021**, *36*, 69–81. https://doi.org/10.1016/S1872-5805(21)60005-7.

18. Thithai, V.; Jin, X.; Ajaz, A.M.; Choi, J.W. Physicochemical properties of activated carbons produced from coffee waste and empty fruit bunch by chemical activation method. *Energies* **2021**, *14*, 3002. https://doi.org/10.3390/en14113002.
19. Danish, M.; Ahmad, T. A review on utilization of wood biomass as a sustainable precursor for activated carbon production and application. *Renew. Sustain. Energy Rev*. **2018**, *87*, 1–21. https://doi.org/10.1016/j.rser.2018.02.003.
20. Balahmar, N.; Al-Jumialy, A.S.; Mokaya, R. Biomass to porous carbon in one step: Directly activated biomass for high performance $CO_2$ storage. *J. Mater. Chem. A* **2017**, *5*, 12330–12339. https://doi.org/10.1039/c7ta01722g.
21. Yin, Z.; Liu, Y.; Liu, S.; Jiang, L.; Tan, X.; Zeng, G.; Li, M.; Liu, S.; Tian, S.; Fang, Y. Activated magnetic biochar by one-step synthesis: Enhanced adsorption and coadsorption for 17β-estradiol and copper. *Sci. Total. Environ.* **2018**, *639*, 1530–1542. https://doi.org/10.1016/j.scitotenv.2018.05.130.
22. Lin, H.L.; Liu, Y.P.; Chang, Z.X.; Yan, S.; Liu, S.C.; Han, S. A new method of synthesizing hemicellulose-derived porous activated carbon for high-performance supercapacitors. *Microporous Mesoporous Mater.* **2020**, *292*, 109707. https://doi.org/10.1016/j.micromeso.2019.109707.
23. Sun, S.N.; Yu, Q.F.; Li, M.; Zhao, H.; Wu, C.X. Preparation of coffee-shell activated carbon and its application for water vapor adsorption. *Renew. Energy* **2019**, *142*, 11–19. https://doi.org/10.1016/j.renene.2019.04.097.
24. Jiang, M.; Zhang, J.L.; Xing, L.B.; Zhou, J.; Cui, H.Y.; Si, W.J.; Zhuo, S.P. KOH-Activated porous carbons derived from chestnut shell with superior capacitive performance. *Chin. J. Chem.* **2016**, *34*, 1093–1102. https://doi.org/10.1002/cjoc.201600320.
25. Mistar, E.M.; Alfatah, T.; Supardan, M.D. Synthesis and characterization of activated carbon from bambusa vulgaris striata using two-step KOH activation. *J. Mater. Res. Technol.* **2020**, *9*, 6278–6286. https://doi.org/10.1016/j.jmrt.2020.03.041.
26. Li, Z.Y.; Gao, X.Y.; Wu, L.; Wang, K.W.; Kobayashi, N. Preparation of activated carbons from poplar wood by chemical activation with KOH. *J. Porous Mater.* **2017**, *24*, 193–202. https://doi.org/10.1007/s10934-016-0252-6.
27. Zhu, X.F.; Luo, Z.J.; Zhu, X.F. Novel insights into the enrichment of phenols from walnut shell pyrolysis loop: Torrefaction coupled fractional condensation. *Waste Manag.* **2021**, *131*, 462–470. https://doi.org/10.1016/j.wasman.2021.07.007.
28. Wang, T.P.; Li, H.; Yuan, J.M.; Li, W.X.; Li, K.; Huang, Y.B.; Xiao, L.P.; Lu, Q. Structures and pyrolytic characteristics of organosolv lignins from typical softwood, hardwood and herbaceous biomass. *Ind. Crops Prod.* **2021**, *171*, 113912. https://doi.org/10.1016/j.indcrop.2021.113912.
29. Wang, J.C.; Kaskel, S. KOH activation of carbon-based materials for energy storage. *J. Mater. Chem.* **2012**, *22*, 23710–23725. https://doi.org/10.1039/C2JM34066F.
30. Xin, Y.; Cao, H.L.; Yuan, Q.X.; Wang, D.L. Two-step gasification of cattle manure for hydrogen-rich gas production: Effect of biochar preparation temperature and gasification temperature. *Waste Manag*. **2017**, *68*, 618–625. https://doi.org/10.1016/j.wasman.2017.06.007.
31. Zhu, X.F.; Li, K.; Zhang, L.Q.; Wu, X.; Zhu, X.F. Comparative study on the evolution of physicochemical characteristics of biochar produced from bio-oil distillation residue under different induction atmosphere. *Energy Convers. Manag*. **2018**, *157*, 288–293. https://doi.org/10.1016/j.enconman.2017.12.010.
32. Zhu, X.F.; Wang, C.; Li, S.S.; Zhu, X.F. Upgrading biochar from bio-oil distillation residue by adding bituminous coal: Effects of induction conditions on physicochemical properties. *Energy Convers. Manag*. **2018**, *174*, 288–294. https://doi.org/10.1016/j.enconman.2018.08.055.
33. Rani, M.U.; Nanaji, K.; Rao, T.N.; Deshpande, A.S. Corn husk derived activated carbon with enhanced electrochemical performance for high-voltage supercapacitors. *J. Power Sources* **2020**, *471*, 228387. https://doi.org/10.1016/j.jpowsour.2020.228387.
34. He, X.; Zeng, K.; Xie, Y.P.; Flamant, G.; Yang, H.P.; Yang, X.Y.; Nzihou, A.; Zheng, A.Q.; Ding, Z.; Chen, H.P. The effects of temperature and molten salt on solar pyrolysis of lignite. *Energy* **2019**, *181*, 407–416. https://doi.org/10.1016/j.energy.2019.05.181.
35. Mueanpun, N.; Srisuk, N.; Chaiammart, N.; Panomsuwan, G. Nanoporous activated carbons derived from water ferns as an adsorbent for removal of paraquat from contaminated water. *Materialia* **2021**, *15*, 100986. https://doi.org/10.1016/j.mtla.2020.100986.
36. Guo, Y.; Wang, Q.Y. Fabrication and Characterization of Activated Carbon from *Phyllostachys edulis* Using Single-Step KOH Activation with Different Temperatures. *Processes* **2022**, *10*, 1712. https://doi.org/10.3390/pr10091712.
37. Khajonrit, J.; Sichumsaeng, T.; Kalawa, O.; Chaisit, S.; Chinnakorn, A.; Chanlek, N.; Maensiri, S. Mangosteen peel-derived activated carbon for supercapacitors. *Prog. Nat. Sci.* **2022**, *32*, 570–578. https://doi.org/10.1016/j.pnsc.2022.09.004.
38. Liu, J.; Li, X.; Weng, W.; Xie, H.; Luo, G.; Niu, Y.; Li, G.; Sun, W. A biomass-derived porous carbon-based nanocomposite for voltammetric determination of quercetin. *Microchim. Acta* **2019**, *186*, 783. https://doi.org/10.1007/s00604-019-3953-0.
39. Zhou, X.Y.; Li, H.C.; Yang, J. Biomass-derived activated carbon materials with plentiful heteroatoms for high-performance electrochemical capacitor electrodes. *J. Energy Chem*. **2016**, *25*, 35–40. https://doi.org/10.1016/j.jechem.2015.11.008.
40. Diao, R.; Zhu, X.F.; Wang, C.; Zhu, X.F. Synergistic effect of physicochemical properties and reaction temperature on gasification reactivity of walnut shell chars. *Energy Convers. Manag*. **2020**, *204*, 112313. https://doi.org/10.1016/j.enconman.2019.112313.
41. Rajasekaran, S.J.; Raghavan, V. Palmyra palm flower biomass-derived activated porous carbon and its application as a supercapacitor electrode. *J. Electrochem. Sci. Eng*. **2022**, *12*, 545–556. https://doi.org/10.5599/jese.1314.

42. Sangeetha, N.M.; Bhat, S.; Raffy, G.; Belin, C.; Loppinet-Serani, A.; Aymonier, C.; Terech, P.; Maitra, U.; Desvergne, J.; Del Guerzo, A. Hybrid materials combining photoactive 2,3-didecyloxyanthracene physical gels and gold nanoparticles. *Chem. Mater.* **2009**, *21*, 3424–3432. https://doi.org/10.1021/cm901225s.
43. Gao, Y.; Yue, Q.Y.; Gao, B.Y.; Li, A.M. Insight into activated carbon from different kinds of chemical activating agents: A review. *Sci. Total Environ*. **2020**, *746*, 141094. https://doi.org/10.1016/j.scitotenv.2020.141094.